applied sciences

MDPI

Article

Layout Optimisation of Frame Structures with Multiple Constraints and Geometric Complexity Control

Yongpeng He *, Paul Shepherd and Jie Wang

Department of Architecture and Civil Engineering, University of Bath, Claverton Down, Bath BA2 7AY, UK
* Correspondence: yh2173@bath.ac.uk

Abstract: A comprehensive framework for the layout optimisation of rigid-jointed frame structures is proposed, addressing multiple mechanical constraints while effectively managing geometric complexity. The constraints considered include displacement, stress, and both local and global stability. Geometric complexity is controlled by minimising low-stiffness elements and reducing the number of elements in the resulting layouts. Numerical examples demonstrate the effectiveness of the proposed method, showcasing its ability to generate optimal structural layouts with desirable mechanical performance and varying levels of geometric complexity in member connectivity. This innovative optimisation framework offers significant advantages over conventional layout optimisation approaches by ensuring both the optimality and manufacturability of frame structures, thereby facilitating their practical application.

Keywords: frame structures; geometric complexity; global stability; layout optimisation; local stability; stress

Citation: He, Y.; Shepherd, P.; Wang, J. Layout Optimisation of Frame Structures with Multiple Constraints and Geometric Complexity Control. *Appl. Sci.* **2024**, *14*, 8157. https://doi.org/10.3390/app14188157

Academic Editor: Valentino Paolo Berardi

Received: 25 July 2024
Revised: 2 September 2024
Accepted: 9 September 2024
Published: 11 September 2024

1. Introduction

The layout optimisation of discrete structures can be traced back to the foundational design theorem proposed by Michell [1], wherein an analytical method for deriving optimal truss layouts was presented. Later, Dorn et al. [2] proposed the ground structure method (GSM) as a numerical approach for determining the optimal layout of discrete structures. The ground structure consists of candidate elements formed by connecting nodes within a specified design domain. Throughout the optimisation process, the cross-sectional areas of these candidate elements can be taken as design variables. An element is eliminated from the ground structure if its cross-sectional area falls below a predefined cut-off threshold, enabling the concurrent optimisation of both size and topology. The resulting optimal layouts have practical applications in guiding the design of diverse engineering structures such as high-rise buildings [3], large-scale roofs [4], long-span bridges [5], etc.

As an alternative, topology optimisation has been applied to continuum structures to achieve optimal material distribution. Unlike discrete-structure layout optimisation, working within a continuum domain broadens the design space, allowing for greater flexibility in shaping the structural components. However, the resulting designs often exhibit varying cross-sections, posing challenges for manufacturing using conventional methods. To mitigate this issue, various strategies have been developed to control design features, such as enforcing the minimum, maximum, and uniform sizes of structural members as demonstrated in the studies of Fernández et al. [6], Liu et al. [7], and Zhang et al. [8]. Furthermore, optimised continuum designs can be converted into discrete structures using topology-preserving skeleton extraction techniques [9,10]. When combined with subsequent shape and sizing optimisation, these methods can significantly enhance constructibility without excessively compromising structural optimality [11]. However, optimising long-span and large-scale structures can be computationally prohibitive due to the fine discretisation required to generate detailed structural elements [12]. Given the

distinct advantages of discrete structures, such as their explicit predefined members in the ground structure and easily controllable cross-sections, this work focuses on layout optimisation of discrete structures, addressing both the manufacturing challenges and the barriers to large-scale applications.

To meet the practical functional requirements, structures must demonstrate satisfactory mechanical performance, particularly in terms of displacement, stress, and stability, while ensuring constructibility by avoiding overly complex designs [13]. This work presents a comprehensive framework for optimising the layout of large-scale frame structures, which offer greater flexibility in forming load paths due to their rotational rigidity compared to trusses [14,15]. The approach integrates multiple mechanical constraints and strategies for controlling geometric complexity. Constraints are applied to displacement, stress, and both local and global stability, while geometric complexity is managed by minimising low-stiffness elements and reducing the number of elements in the resulting layouts. Given that stress and stability (both local and global) involve complex mathematical modelling and exhibit highly non-linear relationships with material configurations, this section reviews current studies on these challenges. Additionally, it provides an overview of the existing methods for controlling geometric complexity in the layout optimisation of discrete structures.

1.1. Precedent Work

1.1.1. Stress

Two main challenges exist for the stress-constrained layout optimisation of discrete structures, namely, stress singularities and the large number of elemental stress constraints. Stress singularity refers to the phenomenon that as the cross-sectional area of an element approaches zero, the corresponding stress constraint should vanish, while the assigned stress limit in the mathematical formulation remains finite. This phenomenon prevents the total removal of elements and hinders the search for true optima [16–18]. To address this issue, the stress constraints for elements with small cross-sectional areas should be relaxed. Several strategies have been proposed for their smooth approximation and relaxation, such as the ϵ-relaxation method [19,20], and smooth envelope functions [18,21]. The second numerical difficulty is associated with the large number of element-wise stress constraints, which requires highly computational-demanding sensitivity analysis, and brings significant challenges to their simultaneous treatment in optimisers. In order to resolve this difficulty, elemental stress constraints can be aggregated into a global measure. Such optimisers then only need to deal with this global measure, as does the sensitivity analysis. Commonly used aggregation functions in stress-constrained optimisation problems include the *K-S* function [22–25], *p*-norm/mean functions [15,26,27], etc. Readers are referred to the aforementioned literature for a detailed introduction and implementation of these aggregation functions.

1.1.2. Local and Global Buckling

Local buckling can be addressed in a manner similar to stress constraints, by limiting element stress below a threshold based on the Euler Buckling criterion [20,28–30], or by adhering to design standards as demonstrated in the works of Mela [31], Cai et al. [32], and He et al. [33]. Consequently, local buckling constraints encounter the same challenges as stress constraints, and can be mitigated through similar approaches. Alternatively, lateral deformation local to elements can be captured using linear buckling analysis by subdividing elements, which allows for the simultaneous treatment of local and global stability [34].

The global stability of structures can be evaluated by linear buckling analysis, which involves solving a generalised eigenvalue problem, formulated with an elastic stiffness matrix and a geometric (stress) stiffness matrix [35]. The fundamental (lowest) eigenvalue obtained is taken as an indicator of global stability. The main challenges associated with global stability-based problems are pseudo (artificial/spurious) buckling modes and

possible clustering and switching between the first several orders of buckling. Pseudo buckling modes mainly derive from the low-stiffness regions, where the geometric stiffness is higher than the elastic stiffness. In order to eliminate pseudo buckling modes, Neves et al. [36] proposed to ignore the geometric stiffness of the low-stiffness material; Bendsøe and Sigmund [37] suggested different interpolation schemes to calculate the material elastic moduli used in the elastic and geometric stiffness matrix. Gao and Ma [38] developed a method based on the modal energy ratio, to identify the pseudo buckling modes in the context of continuum-structure topology optimisation. The same strategy was extended to the stability design of truss and frame structures by Li and Khandelwal [39] and Changizi and Jalalpour [40], respectively. Recently, Zhang et al. [41] proposed a method to mitigate spurious buckling modes by integrating a pseudo mass matrix into the eigenvalue problem. This matrix is constructed based on the status of nodes, characterised by their "nodal density", which is determined as the maximum density among neighbouring elements.

Aside from pseudo buckling modes, the emergence of repeated or closely spaced eigenvalues, and the possible switching between them, also pose great challenges for sensitivity analysis and optimisation. In the case of multiple eigenvalues, when more than one eigenvector is associated with an eigenvalue, these multiple eigenvalues usually do not possess direct differentiable properties, and their sensitivity analysis requires special care [42–44]. Moreover, the switching between the first few eigenvalues, and therefore eigenmodes, which may occur along with material re-distribution, can cause oscillations, and even divergence, to the optimisation problems [37]. For the purpose of ensuring the consistency of the order of eigenvalues (eigenmodes) and, therefore, avoiding multiplicity and rendering them differentiable, Bendsøe and Sigmund [37] recommended imposing consecutive bounding constraints to eigenvalues. As an alternative, the eigenvalues of interest can be transferred into a global measure using aggregation functions [34,45,46], which simultaneously enables differentiability and resolves the dilemma of mode switching. Subsequently, the global measure of eigenvalues, being an approximation to the critical eigenvalue, can be used to guide the stability design of structures [15,34,40,47].

1.1.3. Geometric Complexity Control

The direct results of the layout optimisation of discrete structures may consist of many hair-like features (elements with tiny cross-sectional areas) and present intricate material connectivity, especially when dense ground structures are used. The hair-like features and complicated material connectivity introduce significant challenges to the practical manufacturing of such structures. Typically, the tiny features have negligible mechanical contributions and can be removed if their cross-sectional areas fall below a threshold value. Instead of assigning a static value to the threshold used, Sanders et al. [48] employed adaptive thresholds to simultaneously preserve the optimality of solutions and increase the diversity of structural designs. As an alternative, Parkes [49] suggested a joint cost function and added it to the material cost when measuring the economy of structural designs. The constant joint cost penalises short members [49,50], making them less competitive compared to long members; therefore, during the optimisation process, the optimisers favour the removal of short members. Similar to the joint cost, elemental and nodal fabrication costs have been proposed when assessing the economy or performance of structural designs [51,52]. These cost functions penalise elements with low cross-sectional areas more than those with large cross-sectional areas. As a result, the smaller elements are more prone to removal [51,52]. Additionally, the control of geometric complexity, particularly in terms of simplifying member connectivity in structural layouts, can be enhanced through various methods. For example, intersecting members can be eliminated [53], the number of nodes can be limited [54], and the angles between elements can be restricted [55]. Furthermore, the significant simplification of structural layouts can be achieved by adjusting nodal position and allowing the coalescence of both members and nodes, typically through geometry optimisation methods [50].

1.2. Design Challenges

Despite a substantial body of research dedicated to the layout optimisation of discrete structures, most existing works predominantly address only one or two types of mechanical constraints, and are confined to a limited set of structural elements. For example, Li and Khandelwal [39] focused solely on global stability; Changizi and Jalalpour [40], Mitjana et al. [14], Weldeyesus et al. [56], and Zhao et al. [15] addressed stress and global stability constraints; meanwhile Mela [31] considered stress, and both local and global stability. Additionally, Pedersen and Nielsen [57] investigated optimisation with constraints on displacement, stress, local stability, and eigenfrequency. However, few studies have attempted to simultaneously integrate constraints on displacement, stress, and both local and global stability. An exception is the work by Torii et al. [34], which demonstrated this approach for truss structures with a modest number of elements, leaving its application to large-scale structures unexplored. Large-scale structures, typically optimised using ground structures with refined grid divisions and dense member connectivity, present additional challenges in problem formulation, optimisation convergence, and computational efficiency compared to low-resolution structures.

Furthermore, prevailing approaches for controlling geometric complexity are typically introduced alongside optimisation problems focused on displacement or structural compliance [51,52,54,58]. This raises concerns about their effectiveness in handling multi-constrained problems, particularly when stress and local and global stability constraints are involved. These design-dependent constraints are highly sensitive to changes in design variables and present significant challenges in numerical modelling and convergence [18,21,37,59], such as stress singularities and pseudo buckling modes, especially when the simplification of geometric complexity is coupled with a reduction in element stiffness.

1.3. Contribution of This Work

To address the aforementioned design challenges, this study develops a comprehensive framework for the layout optimisation of frame structures. By simultaneously considering multiple mechanical constraints and controlling geometric complexity, this framework enhances both the design and manufacturability of frame structures. The constraints addressed include displacement, stress, and both local and global stability. Geometric complexity is managed by minimising low-stiffness elements and reducing the number of elements in the resulting layouts. The primary innovation of this study lies in the concurrent handling of multiple mechanical constraints and geometric complexity. Moreover, the proposed method is developed within a gradient-based framework specially tailored for large-scale structures, which involve a large number of degrees of freedom and candidate elements. This approach is particularly advantageous, as such problems are typically challenging to solve using non-gradient based methods like meta-heuristic algorithms.

Regarding the mechanical constraints, displacement and stress are evaluated through linear static analysis, and local and global stability are assessed using linear buckling analysis and element subdivisions. While non-linear structural analysis can provide a more accurate estimation of a structure's load-carrying behaviour, it often requires complex iterative calculations to determine the equilibrium state [60,61]. The sensitivity of mechanical performance metrics, such as the stress, strain, displacement, and buckling load factor, is typically path dependent, necessitating the calculation and storage of structural tangential stiffness and mechanical responses at each load increment [39,62–64]. Additionally, when considering nodal displacement and element stress constraints, the number of constraints usually matches the number of nodes and elements in the structure, leading to a significant computational burden. The high cost of non-linear structural analysis, combined with significant non-linearities in constraints and the complex sensitivity analysis, poses substantial challenges for problem formulation and achieving convergence, especially in large-scale structures with fine grid divisions. Consequently, this study employs linear static and buckling analyses as the primary methods for evaluating structural performance.

These linear analyses are expected to provide valuable insights for optimising material distribution, making them particularly suitable for the conceptual design of frame structures. However, relying on linear analyses may compromise the accuracy and reliability of the optimisation results, especially in scenarios where non-linear effects are significant. To mitigate these risks, a post-optimisation non-linear analysis is recommended to verify structural performance and ensure the safety and robustness of the final designs.

To circumvent the computational demands of analysing numerous node-wise and element-wise constraints, an aggregation technique is employed for each constraint type. This not only streamlines sensitivity analysis but also addresses numerical challenges arising from the non-differentiability of multiple eigenvalues and potential mode switching that can occur in linear buckling analysis. Low-stiffness elements are penalised using the SIMP-based approach [65], therefore driving their removal. To mitigate stress singularities, a *pq* relaxation scheme [26,66] is implemented when formulating stress constraints. Additionally, pseudo buckling modes are eliminated by imposing more severe penalisation to the geometric stiffness matrix compared to the elastic stiffness matrix for low-stiffness elements [47]. Furthermore, an auxiliary component reflecting structural fabrication cost is heuristically combined with material volume to form the objective function. This approach is strategically designed to impose additional penalties on elements, thereby favouring their removal. Consequently, this process significantly influences the overall number of elements and governs the geometric complexity of the resulting structural layouts.

2. Design Variables

This paper focuses on the optimisation of planar frame structures, using 2D beam elements with hollow circular cross-sections for structural simulations. However, the proposed method can be easily extended to 3D, applied to trusses, and adapted to encompass different types of cross-sectional profiles. The hollow circular cross-section is defined by two parameters, the outer diameter d and wall thickness t, with an assumed relationship of $t = d/20$. During the optimisation process, the outer diameters of elements are taken as design variables and are allowed to vary within the range of $[0, d_{\max}]$, where $d_{\max}$ represents the predefined maximum diameter of cross-section.

A threshold parameter d_{th}, typically much smaller than $d_{\max}$, is introduced to differentiate the contribution of elements. Elements with $d_e < d_{\text{th}}$ are termed low-stiffness elements. Moreover, analogous to the density-based topology optimisation of continuum structures, an auxiliary topology variable is defined to indicate the status of elements, which can be expressed as

$$\rho_e = \begin{cases} 1, & \text{if } d_e \geq d_{\text{th}}. \\ d_e/d_{\text{th}}, & \text{otherwise.} \end{cases} \tag{1}$$

where elements with $d_e \geq d_{\text{th}}$ are assigned $\rho_e = 1$, classified as solid elements, and are retained in the layout. Conversely, elements with $d_e = 0$ are assigned $\rho_e = 0$, deemed void, and removed. For elements with $0 < d_e < d_{\text{th}}$, $0 < \rho_e < 1$ is assigned, classifying them as grey elements.

The grey elements should be optimised towards solid or void to minimise their presence. This is achieved using the SIMP-based approach [65], with the penalisation imposed on the elements' cross-sectional diameters rather than the material elasticity modulus as in the original method. The penalised element diameter can be expressed as

$$\tilde{d}_e = \begin{cases} d_e, & \text{if } d_e \geq d_{\text{th}}. \\ {\rho_e}^{\omega} d_{\text{th}}, & \text{otherwise.} \end{cases} \tag{2}$$

where ω is the penalisation factor, usually greater than 1. A larger ω results in more severe penalisation, leading to a drastic decrease in element diameters and effectively driving the removal of grey elements.

The sensitivity of $\tilde{d}_e$ with respect to the design variable is

$$\frac{\partial \tilde{d}_e}{\partial d_e} = \begin{cases} 1, & \text{if } d_e \geq d_{\text{th}}. \\ \omega {\rho_e}^{\omega-1}, & \text{otherwise.} \end{cases} \tag{3}$$

Unless otherwise specified, $d_{\max} = 0.5$ m and $d_{\text{th}} = d_{\max}/10 = 0.05$ m are used as the default values. Given that the wall thickness of the hollow circular cross-section is set to $t = d/20$, the cross-sectional areas and moments of inertia scale with the square and fourth powers of the diameter, respectively. Consequently, the stiffness of elements with $d = d_{\text{th}}$ is approximately 1/10,000 to 1/100 of the stiffness of elements with $d = d_{\max}$. Therefore, elements with $d_e < 0.05$ m, which offer very low stiffness but compromise manufacturability, should be removed during optimisation. Other values for d_{th}, such as $d_{\max}/5$ and $d_{\max}/20$, may be selected depending on stock availability and manufacturing considerations. However, a larger d_{th} might result in an increased number of grey elements ($0 < d_e < d_{\text{th}}$). To prevent abrupt changes in element diameters and sudden removal, and to stabilise the optimisation process, a gradual increase in the penalisation factor ω and a small step size for updating design variables should be employed.

For $d_e \in [0, d_{\max}]$, the values of ρ_e, $\tilde{d}_e$, and $\partial \tilde{d}_e/\partial d_e$ are depicted in Figure 1. As shown in Figure 1a, an increase in ω results in heightened penalisation of d_e, thereby accelerating the removal of low-stiffness elements. Additionally, as illustrated in Figure 1c, discontinuities occur in $\partial \tilde{d}_e/\partial d_e$ when $d_e = d_{\text{th}}$. Integrating smooth Heaviside functions, as demonstrated by Jiang et al. [67], could potentially mitigate this discontinuity; however, it is generally overlooked in this study due to the infrequent occurrence of $d_e = d_{\text{th}}$. Moreover, the optimisation process encounters no noticeable oscillations or difficulties when d_e transitions around d_{th}, suggesting that the discontinuity in $\partial \tilde{d}_e/\partial d_e$ may have minimal impact on the optimisation outcomes.

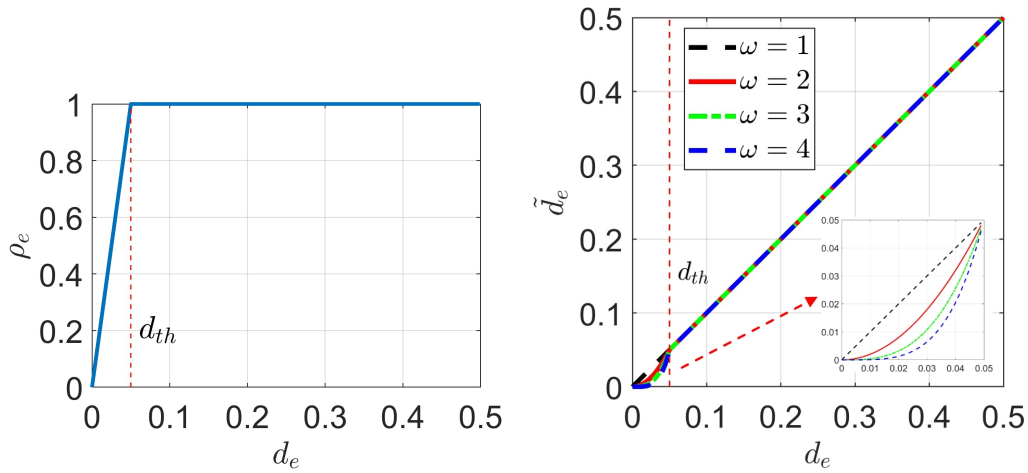

(**a**) ρ_e (**b**) $\tilde{d}_e$

Figure 1. *Cont.*

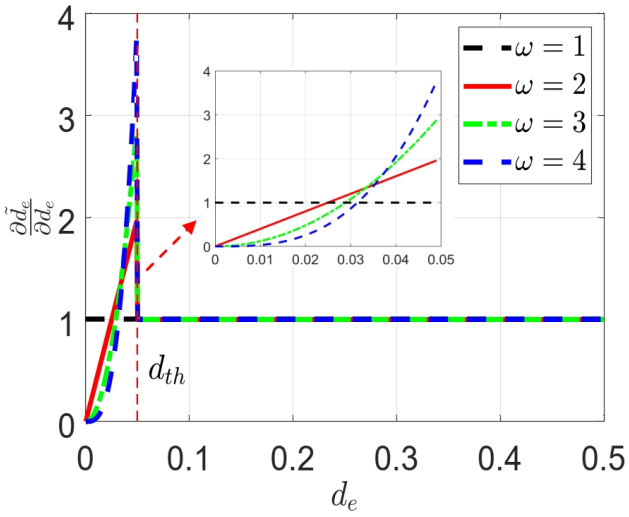

(**c**) $\partial \tilde{d}_e / \partial d_e$

Figure 1. Schematic plots of ρ_e, $\tilde{d}_e$, and $\partial \tilde{d}_e / \partial d_e$.

3. Mechanical Constraints

To guarantee the satisfactory mechanical performance of structures, the optimisation problem within this study incorporates constraints related to displacement, stress, and local and global stability. Additional types of constraints such as dynamic frequency, can be seamlessly integrated, as the calculation and formulation of a structure's natural frequency are similar to those of structural stability. Displacement and stress information can be readily obtained from finite element analysis, while the assessment of both local and global stability necessitates solving an eigenvalue problem formulated with both elastic and geometric stiffness matrices. This section provides formulations for these constraint functions, along with a comprehensive overview of their implementation and sensitivity analysis.

3.1. Displacement

The equilibrium equation for the structure under the external load is

$$\boldsymbol{K}\boldsymbol{U} = \boldsymbol{F} \tag{4}$$

where $\boldsymbol{F}$ is the global force vector, $\boldsymbol{K}$ is the global stiffness matrix, and $\boldsymbol{U}$ is the global displacement vector.

The expression for the differential of the global displacement vector can be derived by differentiating Equation (4) with respect to the design variable d_e, assuming that the global force vector is design independent. This expression can be written as

$$\frac{\partial \boldsymbol{U}}{\partial d_e} = -\boldsymbol{K}^{-1} \frac{\partial \boldsymbol{K}}{\partial d_e} \boldsymbol{U} \tag{5}$$

The displacement constraints ensure that the nodal displacement of the structure under external load remains within specified limits. These constraints can be imposed on displacement in the x and y axes in a 2D context. An example constraint for x-displacement can be expressed as

$$G_i^{U^x} = \frac{|U_i^x|}{\overline{U}^x} \leq 1, \quad i \in [1, n] \tag{6}$$

where $|\cdot|$ represents the absolute value symbol, U_i^x denotes the x displacement of node i, and $\overline{U}^x$ is an upper bound for the x displacement. n is the number of nodes in the structure. U_i^x can be extracted from the global displacement vector:

$$U_i^x = \boldsymbol{I}_{U_i^x} \boldsymbol{U} \tag{7}$$

where $\boldsymbol{I}_{U_i^x}$ is a zero vector with an exceptional entry of 1 at the index corresponding to the x displacement of node i.

The number of x-displacement constraints presented in Equation (6) equals the number of nodes in the structure. To resolve the numerical difficulties caused by the large number of displacement constraints and the associated sensitivity analysis, the node-wise displacement constraints are aggregated into a global measure. Following the idea of Yang and Chen [23] and Le et al. [26], where element-wise stress constraints are aggregated using the p-norm function, the global measure of x-displacement constraints can be expressed as

$$P_{U^x} = \left[\sum_{i=1}^{n} \left(G_i^{U^x} \right)^p \right]^{1/p} \leq 1 \tag{8}$$

where p is the aggregation factor controlling the accuracy of the approximation compared to the actual maximum of $G_i^{U^x}$, and p is usually chosen larger than 1. A large value of p can improve the accuracy of the approximation but also increases non-linearity and may cause numerical instability. Therefore, $p = 4$ is adopted in this work. To allow a more accurate constraint value to be included in optimisation problems, the global measure of x-displacement constraints can be adjusted by making use of the information from the previous optimisation iteration [26]. The normalised global measure of x-displacement constraints can be expressed as

$$\hat{P_{U^x}} = c\, P_{U^x} \leq 1 \tag{9}$$

where c is a normalisation factor calculated at optimisation iteration number I as

$$c^I = \gamma \frac{\max\{|U^x|\}}{P_{U^x}} + (1-\gamma)\, c^{I-1} \tag{10}$$

where c^I and c^{I-1} are the normalisation factors at the current and previous iterations, respectively. The parameter γ modulates the variations between c^I and c^{I-1}, and this work adopts the same value of $\gamma = 0.5$ as used by Le et al. [26].

Based on Equations (5)–(8), the sensitivity of the global displacement constraint with respect to the design variable can be derived as

$$\frac{\partial P_{U^x}}{\partial d_e} = -\left[\sum_{i=1}^{n} \left(G_i^{U^x} \right)^p \right]^{(1/p)-1} \frac{1}{\overline{U}^x} \sum_{i=1}^{n} \operatorname{sign}(U_i^x) \left(G_i^{U^x} \right)^{p-1} \boldsymbol{I}_{U_i^x} \boldsymbol{K}^{-1} \frac{\partial \boldsymbol{K}}{\partial d_e} \boldsymbol{U} \tag{11}$$

where $\operatorname{sign}(\cdot)$ extracts the sign of a value, assigning +1 for a positive input and -1 for a negative input.

By using the adjoint method, Equation (11) can be simplified as

$$\frac{\partial P_{U^x}}{\partial d_e} = -\boldsymbol{V}_{U^x} \frac{\partial \boldsymbol{K}}{\partial d_e} \boldsymbol{U} \tag{12}$$

where $\boldsymbol{V}_{U^x}$ is a virtual displacement vector obtained by solving the system under the virtual load $\boldsymbol{F}_{U^x}$:

$$\boldsymbol{K}\boldsymbol{V}_{U^x} = \overbrace{\left[\sum_{i=1}^{n} \left(G_i^{U^x} \right)^p \right]^{(1/p)-1} \frac{1}{\overline{U}^x} \sum_{i=1}^{n} \operatorname{sign}(U_i^x) \left(G_i^{U^x} \right)^{p-1} \boldsymbol{I}_{U_i^x} \boldsymbol{K}^{-1} \frac{\partial \boldsymbol{K}}{\partial d_e} \boldsymbol{U}}^{\boldsymbol{F}_{U^x}} \tag{13}$$

The y-displacement constraints can be calculated and formulated in the same manner as the x-displacement constraints; however, for the sake of brevity, they are not presented here.

3.2. Stress

The stresses of the 2D beam element are sampled at two end nodes (n_1, n_2). Taking a hollow circular cross-section as an example, the sampling points for stress are shown as red dots in Figure 2.

Figure 2. Stress sampling points for a 2D beam element.

The 2D stress component for element-e at the sampling point-j is

$$\boldsymbol{\sigma}_{e,j} = [\sigma_{e,j}^{xx} \;\; \tau_{e,j}^{xy}]^{\mathrm{T}} = \boldsymbol{B}_{e,j}\boldsymbol{k}_e\boldsymbol{T}_e\boldsymbol{D}_e\boldsymbol{U} \tag{14}$$

where $\boldsymbol{B}_{e,j}$ is a matrix used to calculate stress from the force vector and is constructed based on cross-sectional properties (area, moment of inertial, etc.), $\boldsymbol{k}_e$ represents the element stiffness matrix in the local coordinate system, $\boldsymbol{T}_e$ is the transformation matrix used to transform the element displacement vector from the global coordinate system to local. $\boldsymbol{D}_e$ is a matrix used to extract the element displacement from the global displacement vector. j is the index of the stress sampling point.

Based on Equations (5)–(14), the sensitivity of the stress component with respect to the design variable is

$$\frac{\partial \boldsymbol{\sigma}_{e,j}}{\partial d_e} = \frac{\partial \boldsymbol{B}_{e,j}}{\partial d_e}\boldsymbol{k}_e\boldsymbol{T}_e\boldsymbol{D}_e\boldsymbol{U} + \boldsymbol{B}_{e,j}\frac{\partial \boldsymbol{k}_e}{\partial d_e}\boldsymbol{T}_e\boldsymbol{D}_e\boldsymbol{U} - \boldsymbol{B}_{e,j}\boldsymbol{k}_e\boldsymbol{T}_e\boldsymbol{D}_e\boldsymbol{K}^{-1}\frac{\partial \boldsymbol{K}}{\partial d_e}\boldsymbol{U} \tag{15}$$

The von Mises stress at the sampling point can be calculated from the stress component:

$$\sigma_{e,j}^{\mathrm{vm}} = \sqrt{[\boldsymbol{\sigma}_{e,j}]^{\mathrm{T}}\left[\begin{smallmatrix}1 & 0\\ 0 & 3\end{smallmatrix}\right][\boldsymbol{\sigma}_{e,j}]} \tag{16}$$

The stress constraints formulated based on von Mises stress can be expressed as

$$G_{e,j}^{\sigma^{\mathrm{vm}}} = \frac{\sigma_{e,j}^{\mathrm{vm}}}{\overline{\sigma}^{\mathrm{yield}}} \leq 1, \qquad e \in [1, N],\ j \in [1, 8] \tag{17}$$

where $\overline{\sigma}^{\mathrm{yield}}$ is the predefined yield stress of the material. N is the number of elements in the structure. $j \in [1, 8]$ indicates that there are eight stress sampling points for these elements, four at each end, as shown in Figure 2.

Similar to the node-wise displacement constraints, the element-wise stress constraints are aggregated into a global measure to improve the computational efficiency of the sensitivity analysis. By using the same p-norm function and the same value of $p = 4$, the global measure of stress constraints can therefore be expressed as

$$P_{\sigma^{\mathrm{vm}}} = \left[\sum_{i=1}^{N}\sum_{j=1}^{8}\left(\sigma_{i,j}^{\mathrm{vm}}\right)^p\right]^{1/p} \leq 1 \tag{18}$$

The global measure of stress constraints is normalised in the same way as displacement (Equation (9)) but is omitted here for brevity. Based on Equations (5) and (14)–(18), the sensitivity of the global stress constraint with respect to the design variable can be derived as

$$\frac{\partial P_{\sigma^{\mathrm{vm}}}}{\partial d_e} = \overbrace{\Gamma \sum_{j=1}^{8} \left(\sigma_{e,j}^{\mathrm{vm}}\right)^{p-1} \frac{1}{\overline{\sigma}^{\mathrm{yield}}\, \sigma_{e,j}^{\mathrm{vm}}} \left[\boldsymbol{\sigma}_{e,j}\right]^{\mathrm{T}} \left[\begin{smallmatrix}1&0\\0&3\end{smallmatrix}\right] \left(\frac{\partial \boldsymbol{B}_{e,j}}{\partial d_e} \boldsymbol{k}_e \boldsymbol{T}_e \boldsymbol{D}_e \boldsymbol{U} + \boldsymbol{B}_{e,j} \frac{\partial \boldsymbol{k}_e}{\partial d_e} \boldsymbol{T}_e \boldsymbol{D}_e \boldsymbol{U}\right)}^{1^{\mathrm{st}}\ \mathrm{term}} - \overbrace{\Gamma \sum_{i=1}^{N} \sum_{j=1}^{8} \left(\sigma_{i,j}^{\mathrm{vm}}\right)^{p-1} \frac{1}{\overline{\sigma}^{\mathrm{yield}}\, \sigma_{i,j}^{\mathrm{vm}}} \left[\boldsymbol{\sigma}_{i,j}\right]^{\mathrm{T}} \left[\begin{smallmatrix}1&0\\0&3\end{smallmatrix}\right] \boldsymbol{B}_{i,j} \boldsymbol{k}_i \boldsymbol{T}_i \boldsymbol{D}_i \boldsymbol{K}^{-1} \frac{\partial \boldsymbol{K}}{\partial d_e} \boldsymbol{U}}^{2^{\mathrm{nd}}\ \mathrm{term}} \tag{19}$$

where Γ represents

$$\Gamma = \left[\sum_{i=1}^{N} \sum_{j=1}^{8} \left(\sigma_{i,j}^{\mathrm{vm}}\right)^{p}\right]^{(1/p)-1} \tag{20}$$

By using the adjoint method, the 2nd term in Equation (19) can be simplified as

$$2^{\mathrm{nd}}\ \mathrm{term} = \boldsymbol{V}_{\sigma^{\mathrm{vm}}} \frac{\partial \boldsymbol{K}}{\partial d_e} \boldsymbol{U} \tag{21}$$

where $\boldsymbol{V}_{\sigma^{\mathrm{vm}}}$ is a virtual displacement vector obtained by solving the system under the virtual load $\boldsymbol{F}_{\sigma^{\mathrm{vm}}}$:

$$\boldsymbol{K}\boldsymbol{V}_{\sigma^{\mathrm{vm}}} = \overbrace{\Gamma \sum_{i=1}^{N} \sum_{j=1}^{8} \left(\sigma_{i,j}^{\mathrm{vm}}\right)^{p-1} \frac{1}{\overline{\sigma}^{\mathrm{yield}}\, \sigma_{i,j}^{\mathrm{vm}}} \left[\boldsymbol{\sigma}_{i,j}\right]^{\mathrm{T}} \left[\begin{smallmatrix}1&0\\0&3\end{smallmatrix}\right] \boldsymbol{B}_{i,j} \boldsymbol{k}_i \boldsymbol{T}_i \boldsymbol{D}_i}^{\boldsymbol{F}_{\sigma^{\mathrm{vm}}}} \tag{22}$$

To address the stress singularity associated with low-stiffness elements, a *pq* relaxation scheme is employed [26,66]. This scheme modifies the stress constraints (Equation (17)) based on the auxiliary topology variables of elements:

$$G_{e,j}^{\sigma^{\mathrm{vm}}} = \frac{{\rho_e}^{\eta}\, \sigma_{e,j}^{\mathrm{vm}}}{{\rho_e}^{\nu}\, \overline{\sigma}^{\mathrm{yield}}} = {\rho_e}^{(\eta-\nu)}\, \frac{\sigma_{e,j}^{\mathrm{vm}}}{\overline{\sigma}^{\mathrm{yield}}} \leq 1, \qquad e \in [1, N],\ j \in [1, 8] \tag{23}$$

where ρ_e is given in Equation (1), and η and ν are the penalisation factors for the von Mises stress and the stress limits, respectively. In this work, η is set to the penalisation factor used in Equation (2), and ν is modified accordingly, to maintain a constant relationship of $\eta - \nu = 4$. Following the implementation of stress relaxation, the sensitivity analysis described in Equation (19) can be updated accordingly.

3.3. Stability

Building upon the approach established by Torii et al. [34], the evaluation of both the local and global stability of structures is conducted simultaneously through a linear buckling analysis, where each member is subdivided into several elements to capture the lateral deformation. The formulation of the generalised eigenvalue problem for this linear buckling analysis is

$$[\boldsymbol{K}^{E} + \lambda_j \boldsymbol{K}^{G}]\boldsymbol{\varphi}_j = \boldsymbol{0} \tag{24}$$

where $\boldsymbol{K}^{E}$ is the elastic stiffness matrix, $\boldsymbol{K}^{G}$ is the geometric stiffness matrix, λ_j is the j-th order of the eigenvalue, and $\boldsymbol{\varphi}_j$ is the corresponding eigenvector. $\boldsymbol{\varphi}_j$ is normalised against $\boldsymbol{K}^{E}$ by following ${\boldsymbol{\varphi}_j}^{\mathrm{T}} \boldsymbol{K}^{E} \boldsymbol{\varphi}_k = \delta_{jk}$, and δ_{jk} is Kronecker's delta.

To mitigate pseudo buckling modes caused by low-stiffness elements, the element diameters required for computing the elastic and geometric stiffness matrices are interpo-

lated using different penalisation factors in Equation (2) [47]. Specifically, ω_E is applied to the elastic stiffness matrix, while $\omega_G = \omega_E + 4$ is used for the geometric stiffness matrix.

By introducing an auxiliary variable, $\kappa_j = -1/\lambda_j$, Equation (24) can be rewritten as

$$[\boldsymbol{K}^G - \kappa_j \boldsymbol{K}^E]\boldsymbol{\varphi}_j = \boldsymbol{0} \tag{25}$$

Assuming that the eigenvalue is unimodal, the sensitivity of the auxiliary variable can be expressed as [43]

$$\frac{\partial \kappa_j}{\partial d_e} = -\kappa_j[\boldsymbol{\varphi}_j^{\mathrm{T}} \frac{\partial \boldsymbol{K}^E}{\partial d_e}\boldsymbol{\varphi}_j] + [\boldsymbol{\varphi}_j^{\mathrm{T}} \frac{\partial \boldsymbol{K}^G}{\partial d_e}\boldsymbol{\varphi}_j] - [\boldsymbol{v}_j^{\mathrm{T}} \frac{\partial \boldsymbol{K}^E}{\partial d_e}\boldsymbol{\varphi}_j] \tag{26}$$

where $\boldsymbol{v}_j$ is the virtual displacement vector associated with the virtual load vector $\boldsymbol{F}_j^{\mathrm{Eig}}$. $\boldsymbol{v}_j$ can be obtained by solving the adjoint system:

$$\boldsymbol{K}^E \boldsymbol{v}_j = \boldsymbol{\varphi}_j^{\mathrm{T}} \frac{\partial \boldsymbol{K}^G}{\partial \boldsymbol{U}}\boldsymbol{\varphi}_j = \overbrace{\left[\boldsymbol{\varphi}_j^{\mathrm{T}} \frac{\partial \boldsymbol{K}^G}{\partial U_1}\boldsymbol{\varphi}_j, \boldsymbol{\varphi}_j^{\mathrm{T}} \frac{\partial \boldsymbol{K}^G}{\partial U_2}\boldsymbol{\varphi}_j, \ldots, \boldsymbol{\varphi}_j^{\mathrm{T}} \frac{\partial \boldsymbol{K}^G}{\partial U_m}\boldsymbol{\varphi}_j\right]}^{\boldsymbol{F}_j^{\mathrm{Eig}}} \tag{27}$$

where m is the total number of degrees of freedom of the structure.

To ensure structural stability, the eigenvalues λ_j obtained by solving Equation (24) should be greater than a predefined lower bound $\underline{\lambda}$. Alternatively, by making use of the auxiliary variable κ_j, the stability constraints can be expressed as

$$G_j^{\mathrm{Eig}} = \frac{\kappa_j}{\overline{\kappa}} \leq 1, \quad j \in [1, J] \tag{28}$$

where $\overline{\kappa}$ is defined as $-1/\underline{\lambda}$. J is the highest rank of the under-constrained eigenvalues and is set to 50 in this work.

Similar to the displacement and stress constraints, the stability constraints in Equation (28) are condensed into a global measure using the same aggregation factor of $p = 4$, which can be expressed as

$$P_{\mathrm{Eig}} = \left[\sum_{j=1}^{J} \left(G_j^{\mathrm{Eig}}\right)^p\right]^{1/p} \leq 1 \tag{29}$$

The global measure of stability constraints is normalised to enhance its approximation of the true maximum value, employing a similar approach as applied to the displacement and stress constraints. However, for the sake of simplicity, the expression of this normalisation is not provided here. Based on Equations (25)–(29), the sensitivity of the global measure of the stability constraints with respect to the design variable can therefore be derived as

$$\frac{\partial P_{\mathrm{Eig}}}{\partial d_e} = \left[\sum_{j=1}^{J} \left(G_j^{\mathrm{Eig}}\right)^p\right]^{(1/p)-1} \frac{1}{\overline{\kappa}} \sum_{j=1}^{J} \left(G_j^{\mathrm{Eig}}\right)^{p-1} \frac{\partial \kappa_j}{\partial d_e} \tag{30}$$

4. Problem Formulation

Conventionally, material volume serves as a metric reflecting the economy of a structure. To facilitate control over geometric complexity in structural layouts during the optimisation process, an additional component representing the fabrication cost of the structure is heuristically integrated with material volume to form the objective function. This modified objective function can be expressed as

$$E(\boldsymbol{d}) = \frac{V(\boldsymbol{d})}{V_0} + \alpha \frac{C(\boldsymbol{d})}{C_0} \tag{31}$$

where $V(\boldsymbol{d})$ is the material volume and V_0 is its initial value calculated at the first iteration. $C(\boldsymbol{d})$ represents the fabrication cost and C_0 is its initial value. $\alpha \geq 0$ is a weighting factor.

The structural fabrication cost is obtained by summing up the elemental fabrication cost:

$$C(\boldsymbol{d}) = \sum_{e=1}^{N} \zeta(d_e) \tag{32}$$

where $\zeta(d_e)$ represents the elemental fabrication cost and is approximated by a smooth Heaviside function:

$$\zeta(d_e) = 1 - e^{-\beta\, d_e/d_{\max}} + \frac{d_e}{d_{\max}} e^{-\beta} \tag{33}$$

where β is a parameter controlling the sharpness of the Heaviside projection. The larger the β, the more aggressive the projection. For $d_e \in [0, d_{\max}]$, $\zeta(d_e)$ adopts the value of $[0, 1]$, with 0 indicating the removal and 1, the presence of elements.

The differential of $\zeta(d_e)$ with respect to the design variable is

$$\frac{\partial \zeta(d_e)}{\partial d_e} = \frac{\beta}{d_{\max}} e^{-\beta\, d_e/d_{\max}} + \frac{1}{d_{\max}} e^{-\beta} \tag{34}$$

The plots of $\zeta(d_e)$ and its differential $\partial\zeta(d_e)/\partial d_e$, corresponding to $d_e \in [0, 0.5]$ and different values of β as depicted in Figure 3, reveal that with an increase in β, $\zeta(d_e)$ converges more rapidly towards 1. Moreover, $\partial\zeta(d_e)/\partial d_e$ exhibits higher values for smaller d_e, indicating a more pronounced penalisation of elements with smaller diameters, thereby rendering them more susceptible to removal. In this study, a moderate value of the sharpness parameter is used ($\beta = 8$), in conjunction with different values of the weighting factor α. Through the modulation of α in Equation (31), varying degrees of penalisation, as imposed by the fabrication cost, can be achieved. This adjustment consequently influences the rate at which the values of design variables decrease, implicitly governing the elimination of elements and exerting control over the overall number of elements, i.e., the geometric complexity present in the structural layout.

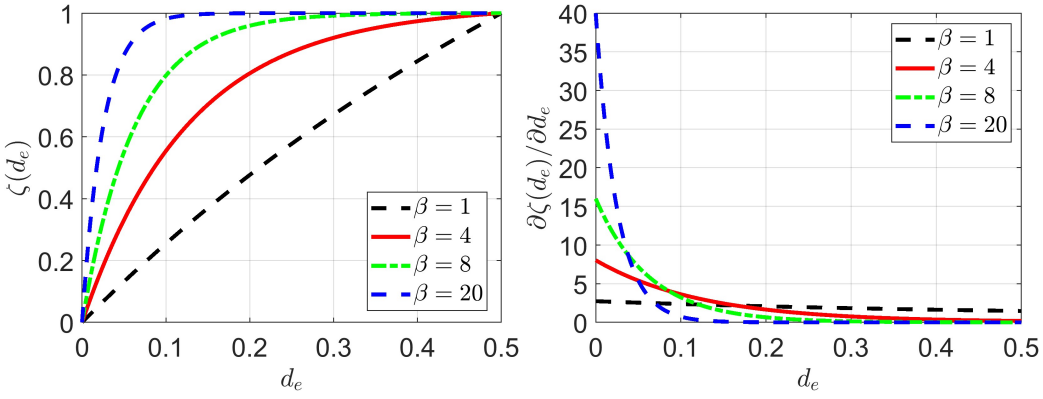

(a) $\zeta(d_e)$ **(b)** $\partial\zeta(d_e)/\partial d_e$

Figure 3. Element fabrication cost and its sensitivity.

Building upon the previously introduced objective and constraint functions, the optimisation problem for the layout of frame structures, incorporating constraints related to displacement, stress, and local and global stability, alongside the modified objective function comprising material volume and fabrication cost of structures, can thus be formulated as

$$\text{Find}: \quad \boldsymbol{d} = [d_1, \ldots, d_e, \ldots, d_N]^{\mathrm{T}},\ d_e \in [0,\ d_{\max}] \tag{35a}$$

$$\min: \quad E(\boldsymbol{d}) = \frac{V(\boldsymbol{d})}{V_0} + \alpha \frac{C(\boldsymbol{d})}{C_0} \tag{35b}$$

$$\text{subject to}: \quad \boldsymbol{KU} = \boldsymbol{F} \tag{35c}$$

$$\hat{P_{U^x}} \leq 1,\ \hat{P_{U^y}} \leq 1 \tag{35d}$$

$$\hat{P_{\sigma^{\mathrm{vm}}}} \leq 1 \tag{35e}$$

$$\hat{P_{\mathrm{Eig}}} \leq 1 \tag{35f}$$

Given the large number of constraints and their highly non-linear relationship with design variables, gradient-based optimisers are employed to solved the problem. Specifically, the Method of Moving Asymptotes (MMA), proposed by Svanberg [68], is adopted. This well-established method has been widely applied in structural optimisation, demonstrating efficient, reliable, and robust performance comparable to other optimisers such as the Interior Point Method and the Sequential Quadratic Programming Method [69,70]. MMA is particularly chosen in this study for its effectiveness in handling multiple constrains and addressing highly non-convex problems.

The sensitivity information of the displacement, stress, and local and global stability constraints as presented in Equations (11), (19) and (30) is validated using the Finite Difference Method (FDM). In each iteration, the values and sensitivity information of the objective and constraint functions are calculated and used by MMA to determine the update directions for the design variables. The step size, governing the maximum allowable change in the design variables per iteration, is restricted to $\varsigma = 0.002$. The optimisation process terminates under two conditions: either the consecutive change in the design variables falls below 1×10^{-5}, or the maximum number of iterations is reached ($maxIter$ = 500). For the interpolation of element diameters to compute the elastic stiffness matrix, the initial penalisation factor ω_E starts at 1.5 and increases by 0.5 every 50 iterations after the 150th iteration, up to a maximum value of 4. Additionally, the penalisation factor ω_G for the geometric stiffness matrix is updated as $\omega_G = \omega_E + 4$. The small step size (ς), the gradual increase in penalisation factors (ω_E and ω_G), and the large number of maximum allowable iterations ($maxIter$) are deliberately chosen to smooth the update of design variables and prevent abrupt change of structural topology. These measures are crucial for handling the inherent non-linearities of the optimisation problem, the high dimensionality of design variables, and the non-convex nature of the design space.

5. Numerical Examples

In this section, three examples are presented to demonstrate the feasibility and effectiveness of the proposed optimisation framework. The first example examines a column subject to a concentrated compressive force on its top edge. The second example explores a short cantilever, while the third focuses on the design of a centrally loaded beam. The first two examples are used as benchmarks to showcase how the framework addresses multiple mechanical constraints and manages the removal of low-stiffness elements. Meanwhile, the third example investigates the impact of member-wise penalisation, influenced by fabrication costs, on minimising the number of elements in the resulting layouts within the context of multi-constrained problems.

Unless otherwise stated, the examples presented adopt identical design parameters. Elements are assigned hollow circular cross-sections, characterised by outer diameters d and wall thickness t, with an assumed relationship of $t = d/20$. An initial cross-section with an outer diameter of $d_{\mathrm{Ini}} = 0.2$ m is adopted. The elasticity modulus of the material is $E = 2 \times 10^5$ MPa, and Poisson's Ratio is $\mu = 0.3$. The displacement constraint is imposed on the vertical displacement, with an upper limit set at $1/400$ of the structural span or height, i.e., $\overline{U}^y = L/400$ or $H/400$. The maximum allowable stress is $\overline{\sigma}^{\mathrm{yield}} = 300$ MPa. When the

local and global stability constraints are included, the minimum allowable buckling load factor is $\underline{\lambda} = 5$.

5.1. Compression Column

The design information of the compression column is illustrated in Figure 4. The design domain measures $L \times H = 8$ m $\times$ 16 m, fixed at the bottom and with a concentrated force acting at the mid-point of the upper surface. The domain is discretised into a grid of 4×8 two-meter wide square cells. Candidate members are formed by interconnecting the internal nodes to their neighbour nodes, and the neighbours of their neighbours, generating a ground structure with two-level connectivity. Additionally, members are split at their intersections as depicted in the amplified view in the middle of Figure 4. This ground structure consists of, in total, 501 nodes and 1292 candidate members. To capture the lateral deformation of members during local buckling in the linear buckling analysis, each member is further subdivided into four elements as shown in the right-end amplified view in Figure 4. This results into a total of 4377 nodes and 5168 elements in the structural analysis.

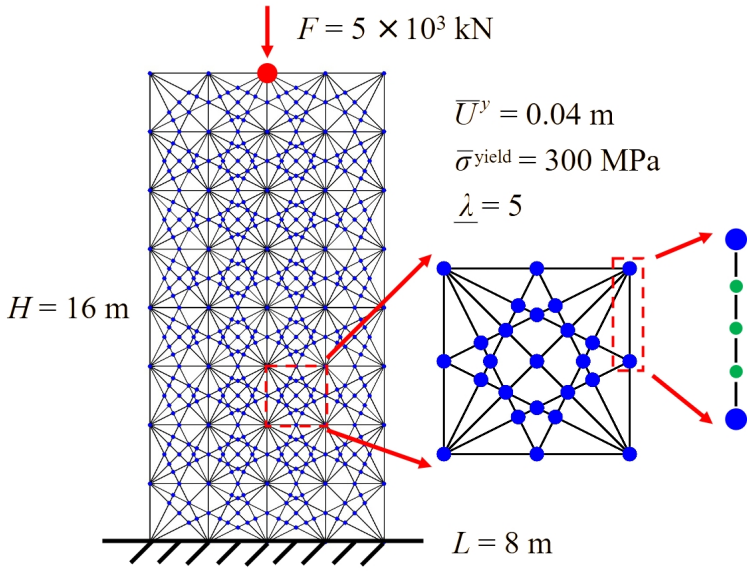

Figure 4. Design information of the compression column.

Four optimisation problems are addressed for the compression column. The first problem considers only displacement and stress constraints, while the remaining three problems incorporate additional global and local stability constraints. These latter problems are differentiated by their methods of treating low-stiffness elements. The second problem employs the SIMP-based scheme with the ω_E initially set to 1.5 and gradually increased up to 4 as described in Section 4. The third problem uses a "hard-kill" scheme, directly removing low-stiffness elements ($\tilde{d}_e < d_{\text{th}}$) during the optimisation. The fourth case disregards the SIMP-based scheme by adopting $\omega_E = 1$ consistently throughout the entire optimisation process. The optimisation results for these four problems are denoted as Layout-I through Layout-IV, respectively. The optimal structures and the corresponding first three buckling modes are depicted in Figure 5, where red lines signify compression elements, blue lines represent tension elements, and black lines denote grey elements with diameters ($\tilde{d}_e$) falling into the range of $(0, d_{\text{th}})$.

As shown in Figure 5a, Layout-I presents a simple vertical bar. In this layout, stress constraints dominate over displacement constraints, resulting in a uniform cross-section with a diameter of $\tilde{d} = 0.334$ m. The corresponding cross-sectional area and moment of inertia are $A = 0.0167$ m^2 and $I = 2.106 \times 10^{-4}$ m^4, respectively. The buckling load factors and modes align with the results of the theoretical Euler buckling analysis for a column

with fixed-free ends. The critical load is given by $P_{cr} = \frac{\kappa^2 \pi^2 EI}{4H^2}$, where $\kappa = 1, 3, 5$ for the first, second, and third buckling modes, respectively.

As depicted in Figure 5b–d, incorporating global and local stability constraints leads to Layout-II, -III, and -IV, which feature additional elements providing lateral support. The buckling modes exhibit concurrent nodal movement and in-member lateral displacement, demonstrating the feasibility of using linear buckling analysis with element refinement to capture both local and global buckling. Moreover, these modes mostly correspond to solid elements ($\tilde{d}_e \geq d_{th}$), highlighting the effectiveness of imposing distinct penalisation to the elastic and geometric stiffness in suppressing pseudo buckling modes. Furthermore, Layout-II, -III, and -IV share similarities with the designs presented in the works of Li and Khandelwal [39], Changizi and Jalalpour [40], and Poulsen et al. [71], where the stability properties were also considered. However, quantitative comparisons are not feasible due to differences in the optimisation problems, as this study integrates multiple mechanical constraints that are not addressed in the aforementioned works. Notably, the optimal layouts generated using discrete structures are generally different from those using continuum structures. The latter usually manifest as two primary inclined components augmented with secondary lateral bracing as presented in the works of Gao and Ma [38], Ferrari et al. [47], and Dahlberg et al. [72]. Investigating the reasons behind these differences and conducting a quantitative comparison of these layouts is of interest but is left for future study.

The material volume (V), number of elements (n), maximum y displacement (U^y_{max}), maximum von Mises stress σ^{vm}_{max}, and fundamental buckling load factor (λ_1) for the four structural layouts are summarised in Table 1. All layouts exhibit satisfactory mechanical performance when the relevant constraints are included in the optimisation problems. To further illustrate the superior stability of Layout-II, -III, and -IV over Layout-I, a separate sizing optimisation is conducted on Layout-I while incorporating both the global and local stability constraints. In this context, the upper bound limit on element diameters is relaxed to allow for increases as necessary to satisfy the stability constraints. This optimisation results in a structure that retains the same layout but features a cone-shaped cross-section, with element diameters tapering from 1.01 m at the bottom to 0.433 m at the top. Consequently, the material volume of the resulting structure is 1.820 m^3, which is more than 4.2, 3.6, and 4.4 times that of Layout-II, -III, and -IV, respectively.

Among the designs with stability constraints, Layout-IV, which was developed without penalising low-stiffness elements, exhibits a considerable number of grey elements, thereby substantially impairing its manufacturability. This observation aligns with findings from prior research on discrete-structure layout optimisation, which have separately explored various constraints such as stress [1,49,50,73], displacement [51], compliance [52], and stability [39,40,71]. The presence of a significant number of elements, including those of low stiffness, in the resultant layouts can be attributed to the inherent tendency of the ground structure method to produce non-unique maximum stiffness designs [74]. Nevertheless, upon visually examining Layout-II and -IV and comparing their material usage, it becomes evident that implementing the SIMP-based scheme effectively reduces the occurrence of grey elements without excessively compromising economic feasibility, although some residual grey elements may persist. Notably, addressing these residual elements could potentially benefit from the density projection scheme developed in continuum-structure topology optimisation [75].

Furthermore, the discrepancy in material volume between Layout-II and -III highlights that employing the SIMP-based scheme to handle low-stiffness elements leads to a more efficient layout with decreased material consumption compared to the "hard-kill" approach. Therefore, it can be concluded that the SIMP-based scheme is appropriate for minimising low-stiffness elements, thereby improving manufacturability while maintaining the optimality of the resulting layouts.

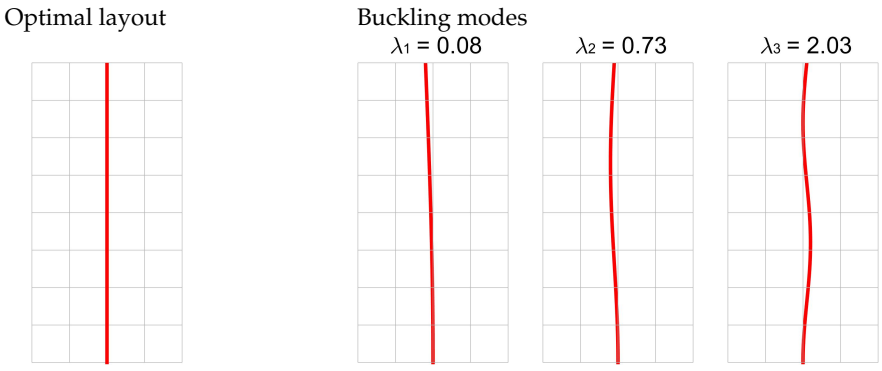

(**a**) Layout-I, considers only displacement and stress constraints

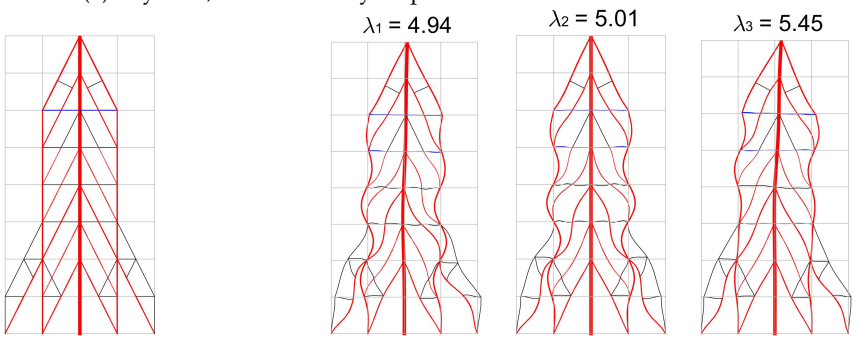

(**b**) Layout-II, considers all constraints and adopts $\omega_E = 1.5 \sim 4$

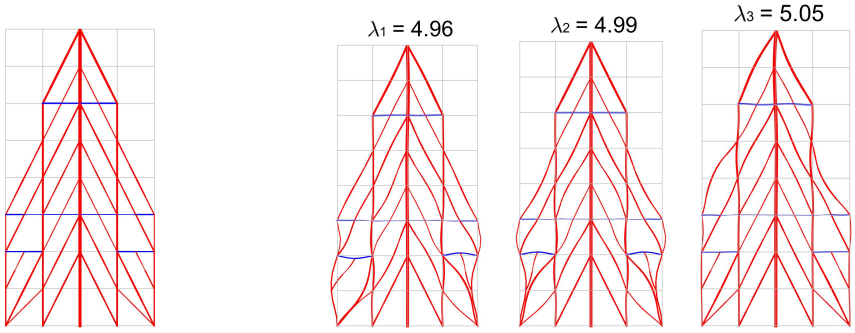

(**c**) Layout-III, considers all constraints and directly remove low-stiffness elements

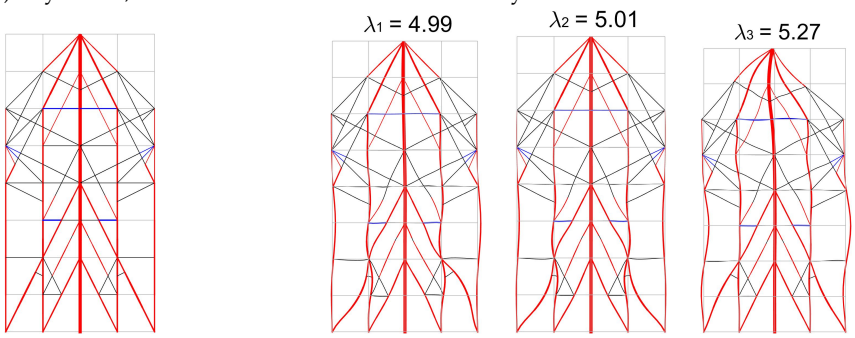

(**d**) Layout-IV, considers all constraints and adopts $\omega_E = 1$ consistently

Figure 5. Optimal layouts and buckling modes of the compression column. (For interpretation of the references to colour in this figure legend, the reader is referred to the web version of this article).

Table 1. Geometric and mechanical properties of the optimal layouts of the compression column.

Layout	V/m^3	U^y_{max}/m	σ^{vm}_{max}/MPa	λ_1	n
I	0.267	0.024	300	0.08	64
II	0.431	0.017	300	4.94	1000
III	0.496	0.018	300	4.96	1032
IV	0.407	0.021	300	4.99	1368

5.2. Short Cantilever

The short cantilever example has dimensions of $L \times H = 12\ m \times 24\ m$ as shown in Figure 6. It is fixed at the top and bottom left nodes and subject to a concentrated vertical force applied at the right middle. The domain is discretised into 4×8 three-meter-wide square cells. Similar to the compression column, a ground structure with two-level connectivity is employed, where members are split at their intersections, and each is subdivided into four elements for structural analysis. This ground structure comprises the same number of nodes and members as the compression column.

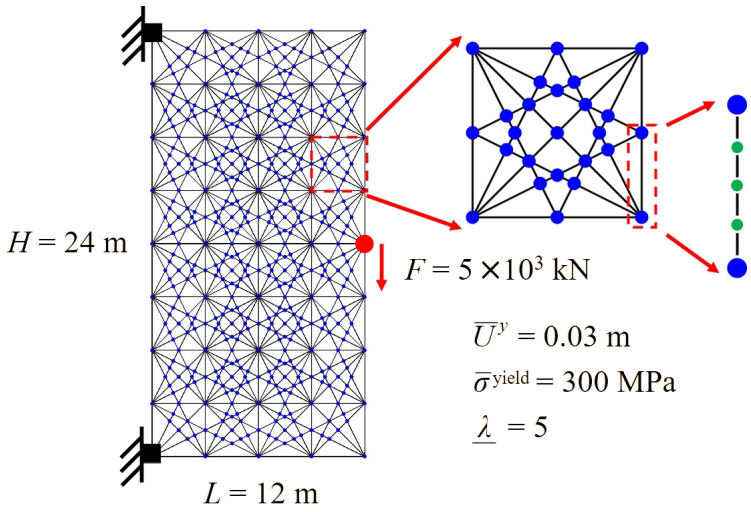

Figure 6. Design information of the short cantilever.

Similarly, three optimisation problems are tackled: the first focuses solely on displacement and stress constraints, and the second incorporates additional global and local stability constraints, while the third considers all constraints and employs the hard-kill scheme to remove low-stiffness elements during the optimisation process. The resulting optimal structures are denoted as Layout-I, -II, and -III, respectively, and are depicted in Figure 7, along with their buckling modes. Layout-I presents a simple two-bar structure, with one compression and one tension bar, Layout-II and -III include additional elements concentrated at the lower part of the structure to reinforce the compression zone. Both Layout-II and -III exhibit similarities to the results presented in previous works such as Ferrari and Sigmund [76] and Weldeyesus et al. [77].

The material volume, mechanical performance metrics, and number of elements for Layout-I, -II, and -III are summarised in Table 2. All layouts demonstrate satisfactory mechanical performance when relevant constraints are incorporated in the optimisation problem. A separate sizing optimisation is performed on Layout-I with the inclusion of additional global and local stability constraints. The resulting layout consumes a material volume of $0.758\ m^3$, which is more than 1.2 and 1.1 times that of Layout-II and -III, respectively. This indicates that the member configurations in Layout-II and -III are more optimal than that in Layout-I by considering the stability properties during the optimisation. Furthermore, the material volume of Layout-II is less than that of Layout-III, despite the former presenting more elements. This demonstrates the effectiveness of the SIMP-

based scheme over the "hard-kill" scheme when treating low-stiffness elements in the optimisation process.

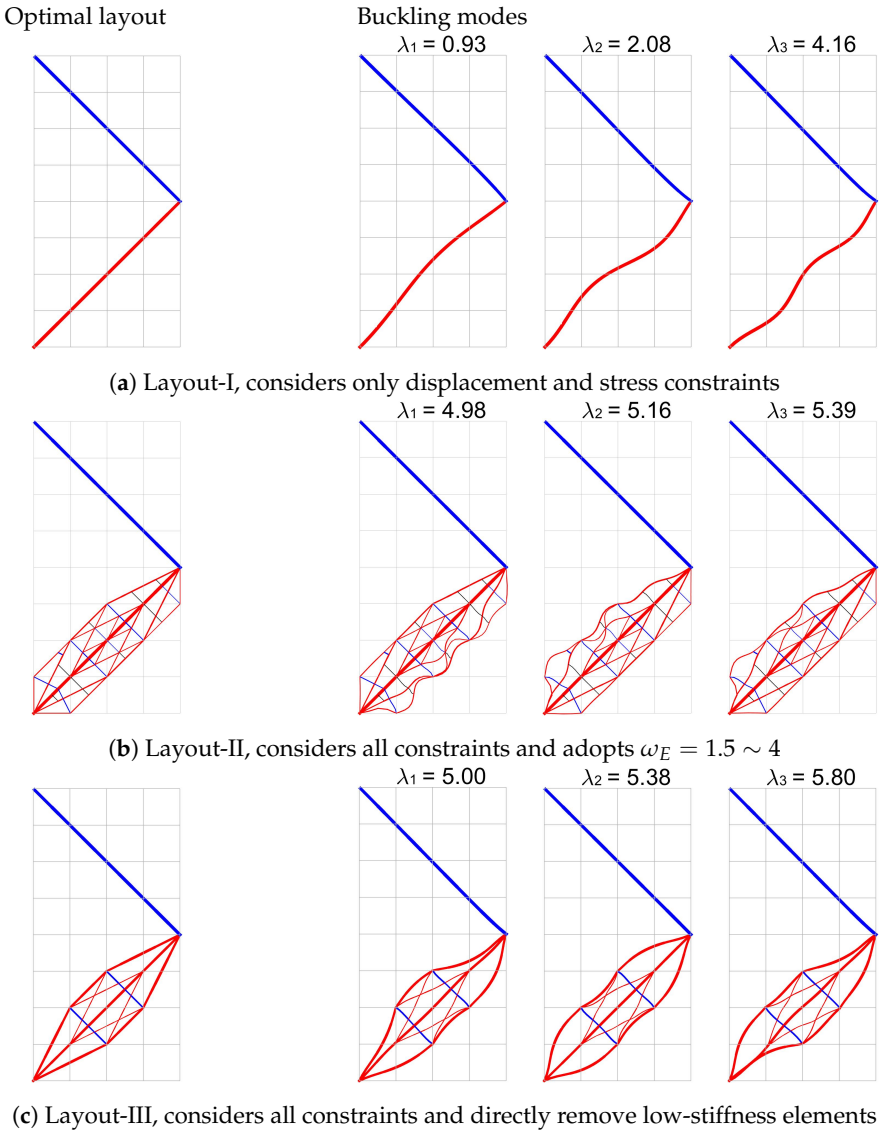

(**a**) Layout-I, considers only displacement and stress constraints

(**b**) Layout-II, considers all constraints and adopts $\omega_E = 1.5 \sim 4$

(**c**) Layout-III, considers all constraints and directly remove low-stiffness elements

Figure 7. Optimal layouts and buckling modes of the short cantilever. (For interpretation of the references to colour in this figure legend, the reader is referred to the web version of this article).

Table 2. Geometric and mechanical information on the optimal layouts of the short cantilever.

Layout	V/m^3	$U^y_{\max}$/m	$\sigma^{vm}_{\max}$/MPa	λ_1	n
I	0.483	0.03	300	0.93	120
II	0.611	0.027	300	4.98	652
III	0.685	0.026	300	5	468

5.3. Centrally Loaded Beam

The design of the centrally loaded beam is depicted in Figure 8. This structure is fixed at the left and right bottom nodes, with a concentrated vertical force acting at the middle bottom. The design domain measures $L \times H = 48$ m $\times$ 16 m and is discretised into 12×4 four-meter-wide square cells. A ground structure with two-level connectivity is employed, where members are split at their intersections. The ground structure comprises a total of 773 nodes and 1996 candidate members. In order to capture member instability

using linear buckling analysis, each member is further divided into four elements, resulting in a structural model with 6761 nodes and 7984 elements.

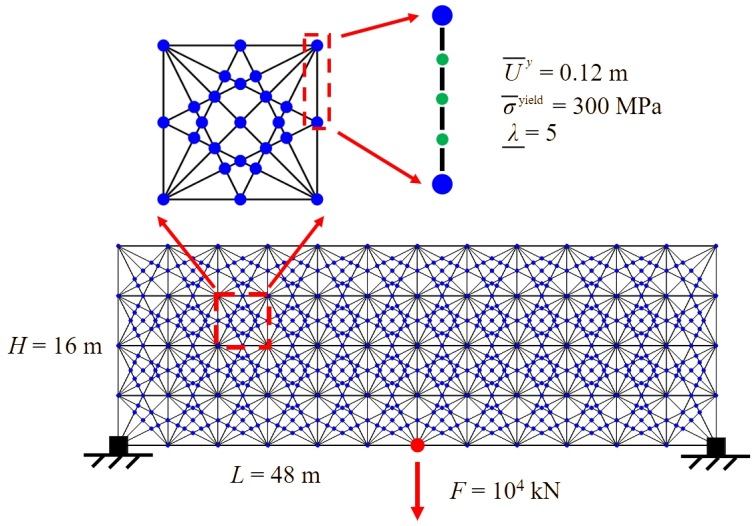

Figure 8. Design information of the centrally loaded beam.

Six optimisation problems are conducted for the centrally loaded beam. The first problem considers only displacement and stress constraints, while the remaining five integrate additional global and local stability constraints. The second problem employs the SIMP-based scheme to drive the removal of low-stiffness elements, whereas the third problem directly removes them using a "hard-kill" scheme. The fourth, fifth, and sixth problems also employ the SIMP-based scheme but incorporate the structural fabrication cost as described in Equation (31), using weighting factor $\alpha = 1$, 2, and 5, respectively. To ensure that the artificial member-wise penalisation caused by structural fabrication cost does not influence the early stages of the optimisation process, the SIMP-based scheme is activated starting from the 150th iteration. The resulting layouts of these six problems are termed Layout-I through VI, and are depicted in Figure 9, alongside their fundamental buckling modes. Additionally, their geometric properties and mechanical performance metrics are summarised in Table 3.

Table 3. Geometric and mechanical properties of the optimal layouts of the centrally loaded beam.

Layout	V/m^3	U^y_{max}/m	σ^{vm}_{max}/MPa	λ_1	n	α
I	2.300	0.089	300	0.74	280	0
II	3.559	0.064	300	4.91	2728	0
III	3.739	0.062	300	4.96	2480	0
IV	3.677	0.062	300	4.93	1944	1
V	4.018	0.056	300	4.99	1544	2
VI	4.568	0.050	300	4.98	1248	5

As illustrated in Figure 9a, Layout-I presents as a simple structure comprising a primary arch system and two hanging bars connecting the load point to the arch. This design closely resembles the results of truss layout optimisation, which could be readily reproduced using the code provided by Zegard and Paulino [78]. Furthermore, with the incorporation of both global and local stability constraints, Layout-II–VI share common features such as radially arranged tension elements from the load point and a primary arch system braced by short members. Quantitatively comparing the existing optimisation results from the literature remains challenging due to the scarcity of research on multi-constrained layout optimisation for frame structures, particularly in scenarios involving numerous candidate elements. To evaluate the optimality of the obtained structural layouts, a stability-constrained topology

optimisation problem is addressed in the context of continuum structures using the code provided by Ferrari et al. [47]. The result, depicted in Figure 10, exhibits qualitative similarities to Layout-II–VI, thereby suggesting the optimality of these solutions.

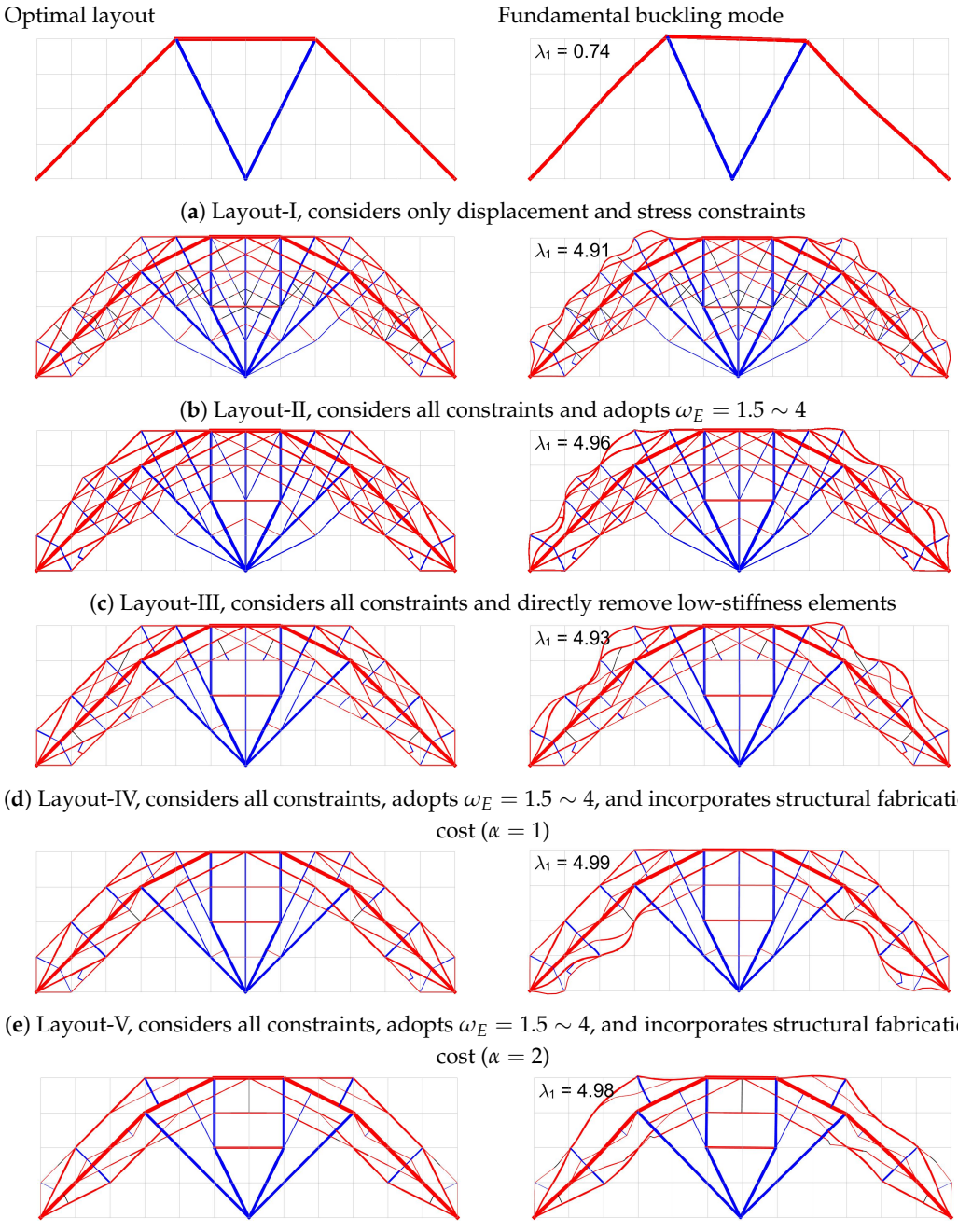

(**a**) Layout-I, considers only displacement and stress constraints

(**b**) Layout-II, considers all constraints and adopts $\omega_E = 1.5 \sim 4$

(**c**) Layout-III, considers all constraints and directly remove low-stiffness elements

(**d**) Layout-IV, considers all constraints, adopts $\omega_E = 1.5 \sim 4$, and incorporates structural fabrication cost ($\alpha = 1$)

(**e**) Layout-V, considers all constraints, adopts $\omega_E = 1.5 \sim 4$, and incorporates structural fabrication cost ($\alpha = 2$)

(**f**) Layout-VI, considers all constraints, adopts $\omega_E = 1.5 \sim 4$, and incorporates structural fabrication cost ($\alpha = 5$).

Figure 9. Optimal layouts and buckling modes of the centrally loaded beam. (For interpretation of the references to colour in this figure legend, the reader is referred to the web version of this article).

Additionally, a comparison between Layout-II and -III reveals that the SIMP-based scheme produces a lighter-weight structure compared to the "hard-kill" scheme. This advantage stems from the SIMP-based scheme's ability to gradually remove low-stiffness elements while allowing for their reintroduction as necessary during the optimisation process.

Moreover, there is a noticeable decreasing trend in the number of elements among Layout-II, -IV, -V, and -VI, highlighting the effectiveness of integrating the structural

fabrication cost into the objective function to promote element removal and simplify geometric complexity. However, there is also an evident increase in material consumption across these layouts, indicating that the inclusion of fabrication cost could potentially compromise design optimality. This is due to the heightened sensitivity of the objective function caused by member-wise penalisation from fabrication costs, which may diminish the influence of constraint function sensitivities and thereby adversely affect the direction of design variable updates during optimisation.

Figure 10. An optimal centrally loaded beam obtained by running the code provided by Ferrari et al. [47].

6. Discussion

This section evaluates the computational efficiency of the proposed optimisation framework and discusses the optimality of the resulting layouts.

6.1. Computational Efficiency

The proposed optimisation framework was developed using MATLAB. All optimisation problems were executed on a laptop PC equipped with an Intel i7-8750H CPU, utilising parallel processing across four cores. The number of elements in these examples ranged from 5000 to 8000. On average, each optimisation iteration required approximately 10 s of CPU time, allowing the problems to be solved within one or two hours. However, as the number of nodes and elements increases, the computational demand grows exponentially. For instance, numerical experiments show that in optimising a compression column with three-level connectivity, the number of nodes and elements rises to 24,673 and 29,024, respectively, resulting in an average CPU time per iteration exceeding 5 min. While both linear static analysis and eigenvalue buckling analysis are completed within seconds, sensitivity analysis is the most time-consuming step, followed by the updates of design variables. This is due to the need to loop over all constrained nodes for displacement constraints, all elements for stress constraints, and all buckling modes for stability constraints as described by Equations (11), (19) and (30). This presents significant challenges for complex, large-scale structures, such as spatial frames, where the number of candidate elements increases dramatically with finer domain discretisations and higher levels of member connectivity.

6.2. Optimality of the Resulting Layouts

The layouts for the three structures optimised using the proposed framework exhibit satisfactory mechanical performance and notable improvements in manufacturability. However, these designs may only represent the local optima due to the high non-linearity of the constraints, which are sensitive to material distributions and may conflict with one another, increasing the risk of converging to suboptimal solutions. While finer grid discretisations and higher member connectivity could potentially improve design optimality, they also lead to increased computational costs and more complex final layouts. To balance optimality, manufacturability, and efficiency, further investigation is needed. This could involve starting with simpler, suboptimal structures that meet basic mechanical constraints such as displacement and stress, and then progressively incorporating stability considerations while strategically refining grid discretisation and adjusting member connectivity.

7. Conclusions

This study presents a comprehensive framework for optimising the layout of frame structures, addressing various practical mechanical constraints while effectively managing

geometric complexity. Constraints related to displacement, stress, and both local and global stability are consolidated into aggregation expressions, enhancing computational and optimisation efficiency for large-scale applications. To manage geometric complexity, the framework employs a SIMP-based approach to minimise the presence of low-stiffness elements. Additionally, fabrication cost-based penalisation is incorporated to reduce the total number of elements, which simplifies member connectivity and enhances the interpretability and manufacturability of the final layouts. The effectiveness of this framework is demonstrated through its application to large-scale 2D frame structures containing thousands of candidate elements. The design solutions demonstrate satisfactory mechanical performance and practical constructibility characterised by minimal low-stiffness elements and enhanced geometric simplification. However, further work is needed to improve the computational efficiency and design optimality. Future studies could explore progressive and local domain discretisation techniques and member addition strategies, within a multi-constrained framework.

Author Contributions: Conceptualization, Y.H.; methodology, Y.H.; software, Y.H.; validation, Y.H.; formal analysis, Y.H.; investigation, Y.H.; resources, Y.H.; data curation, Y.H.; writing—original draft preparation, Y.H.; writing—review and editing, P.S. and J.W.; visualization, Y.H.; supervision, P.S. and J.W.; funding acquisition, Y.H. All authors have read and agreed to the published version of the manuscript.

Funding: The first author receives support from Chinese Scholarship Council (CSC) through the CSC-University of Bath Joint Scholarship.

Institutional Review Board Statement: Not applicable.

Informed Consent Statement: Not applicable.

Data Availability Statement: The data that support the findings of this study are available from the corresponding author upon reasonable request.

Acknowledgments: The sharing of the MMA code from Krister Svanberg is gratefully acknowledged.

Conflicts of Interest: The authors declare that they have no conflicts of interest.

References

1. Michell, A. LVIII. The limits of economy of material in frame-structures. *Lond. Edinb. Dublin Philos. Mag. J. Sci.* **1904**, *8*, 589–597. [CrossRef]
2. Dorn, W.S.; Gomory, R.E.; Greenberg, H.J. Automatic design of optimal structures. *J. Mec.* **1964**, *3*, 25–52.
3. Zegard, T.; Paulino, G.H. GRAND3—Ground structure based topology optimization for arbitrary 3D domains using MATLAB. *Struct. Multidiscip. Optim.* **2015**, *52*, 1161–1184. [CrossRef]
4. Tugilimana, A.; Filomeno Coelho, R.; Thrall, A.P. Including global stability in truss layout optimization for the conceptual design of large-scale applications. *Struct. Multidiscip. Optim.* **2018**, *57*, 1213–1232. [CrossRef]
5. Fairclough, E.H.; Gilbert, M. Layout optimization of long-span structures subject to self-weight and multiple load-cases. *Struct. Multidiscip. Optim.* **2022**, *65*, 197. [CrossRef]
6. Fernández, E.; Yang, K.k.; Koppen, S.; Alarcón, P.; Bauduin, S.; Duysinx, P. Imposing minimum and maximum member size, minimum cavity size, and minimum separation distance between solid members in topology optimization. *Comput. Methods Appl. Mech. Eng.* **2020**, *368*, 113157. [CrossRef]
7. Liu, J.; Li, L.; Ma, Y. Uniform thickness control without pre-specifying the length scale target under the level set topology optimization framework. *Adv. Eng. Softw.* **2018**, *115*, 204–216. [CrossRef]
8. Zhang, W.; Li, D.; Zhang, J.; Guo, X. Minimum length scale control in structural topology optimization based on the Moving Morphable Components (MMC) approach. *Comput. Methods Appl. Mech. Eng.* **2016**, *311*, 327–355. [CrossRef]
9. Nana, A.; Cuillière, J.C.; Francois, V. Automatic reconstruction of beam structures from 3D topology optimization results. *Comput. Struct.* **2017**, *189*, 62–82. [CrossRef]
10. Gamache, J.F.; Vadean, A.; Noirot-Nérin, É.; Beaini, D.; Achiche, S. Image-based truss recognition for density-based topology optimization approach. *Struct. Multidiscip. Optim.* **2018**, *58*, 2697–2709. [CrossRef]
11. Yin, G.; Xiao, X.; Cirak, F. Topologically robust CAD model generation for structural optimisation. *Comput. Methods Appl. Mech. Eng.* **2020**, *369*, 113102. [CrossRef]
12. Aage, N.; Andreassen, E.; Lazarov, B.S. Topology optimization using PETSc: An easy-to-use, fully parallel, open source topology optimization framework. *Struct. Multidiscip. Optim.* **2015**, *51*, 565–572. [CrossRef]

13. Cucuzza, R.; Aloisio, A.; Rad, M.M.; Domaneschi, M. Constructability-based design approach for steel structures: From truss beams to real-world inspired industrial buildings. *Autom. Constr.* **2024**, *166*, 105630. [CrossRef]
14. Mitjana, F.; Cafieri, S.; Bugarin, F.; Gogu, C.; Castanie, F. Optimization of structures under buckling constraints using frame elements. *Eng. Optim.* **2019**, *51*, 140–159. [CrossRef]
15. Zhao, L.; Yi, J.; Zhao, Z.; Zhang, Z.; Han, Y.; Rong, J. Topology optimization of frame structures with stress and stability constraints. *Struct. Multidiscip. Optim.* **2022**, *65*, 268. [CrossRef]
16. Kirsch, U. On singular topologies in optimum structural design. *Struct. Optim.* **1990**, *2*, 133–142. [CrossRef]
17. Cheng, G.; Jiang, Z. Study on topoogy optimization with stress constraints. *Eng. Optim.* **1992**, *20*, 129–148. [CrossRef]
18. Rozvany, G.I. On design-dependent constraints and singular topologies. *Struct. Multidiscip. Optim.* **2001**, *21*, 164–172. [CrossRef]
19. Cheng, G.D.; Guo, X. ϵ-relaxed approach in structural topology optimization. *Struct. Optim.* **1997**, *13*, 258–266. [CrossRef]
20. Guo, X.; Cheng, G.; Yamazaki, K. A new approach for the solution of singular optima in truss topology optimization with stress and local buckling constraints. *Struct. Multidiscip. Optim.* **2001**, *22*, 364–373. [CrossRef]
21. Rozvany, G.I.N. Difficulties in truss topology optimization with stress, local buckling and system stability constraints. *Struct. Optim.* **1996**, *11*, 213–217. [CrossRef]
22. Kreisselmeier, G.; Steinhauser, R. Systematic Control Design by Optimizing a Vector Performance Index. *Ifac Proc. Vol.* **1979**, *12*, 113–117. [CrossRef]
23. Yang, R.J.; Chen, C.J. Stress-based topology optimization. *Struct. Optim.* **1996**, *12*, 98–105. [CrossRef]
24. París, J.; Navarrina, F.; Colominas, I.; Casteleiro, M. Topology optimization of continuum structures with local and global stress constraints. *Struct. Multidiscip. Optim.* **2009**, *39*, 419–437. [CrossRef]
25. Luo, Y.; Wang, M.Y.; Kang, Z. An enhanced aggregation method for topology optimization with local stress constraints. *Comput. Methods Appl. Mech. Eng.* **2013**,*254*, 31–41. [CrossRef]
26. Le, C.; Norato, J.; Bruns, T.; Ha, C.; Tortorelli, D. Stress-based topology optimization for continua. *Struct. Multidiscip. Optim.* **2010**, *41*, 605–620. [CrossRef]
27. Verbart, A.; Langelaar, M.; van Keulen, F. A unified aggregation and relaxation approach for stress-constrained topology optimization. *Struct. Multidiscip. Optim.* **2017**, *55*, 663–679. [CrossRef]
28. Achtziger, W. Local stability of trusses in the context of topology optimization Part I: Exact modelling. *Struct. Optim.* **1999**, *17*, 235–246.
29. Achtziger, W. Local stability of trusses in the context of topology optimazation. Part II: A numerical approach. *Struct. Optim.* **1999**, *17*, 247–258.
30. Guo, X.; Cheng, G.D.; Olhoff, N. Optimum design of truss topology under buckling constraints. *Struct. Multidiscip. Optim.* **2005**, *30*, 169–180. [CrossRef]
31. Mela, K. Resolving issues with member buckling in truss topology optimization using a mixed variable approach. *Struct. Multidiscip. Optim.* **2014**, *50*, 1037–1049. [CrossRef]
32. Cai, Q.; Feng, R.; Zhang, Z. Topology optimization of trusses incorporating practical local buckling stability considerations. *Structures* **2022**, *41*, 1710–1718. [CrossRef]
33. He, F.; Feng, R.; Cai, Q. Topology optimization of truss structures considering local buckling stability. *Comput. Struct.* **2024**, *294*, 64–73. [CrossRef]
34. Torii, A.; Lopez, J.R.H.; Miguel, L.F. Modeling of global and local stability in optimization of truss-like structures using frame elements. *Struct. Multidiscip. Optim.* **2015**, *51*, 1187–1198. [CrossRef]
35. Cook, R.D.; Malkus, D.S.; Plesha, M.E.; Witt, R.J. *Concepts and Applications of Finite Element Analysis*; John Wiley & Sons: Hoboken, NJ, USA, 2007.
36. Neves, M.; Rodrigues, M.H.; Guedes, J.M. Generalized topology design of structures with a buckling load criterion. *Struct. Optim.* **1995**, *10*, 71–78. [CrossRef]
37. Bendsøe, M.P.; Sigmund, O. *Topology Optimization, Theory, Method and Applications*; Springer: Berlin/Heidelberg, Germany, 2004.
38. Gao, X.; Ma, H. Topology optimization of continuum structures under buckling constraints. *Comput. Struct.* **2015**, *157*, 142–152. [CrossRef]
39. Li, L.; Khandelwal, K. Topology optimization of geometrically nonlinear trusses with spurious eigenmodes control. *Eng. Struct.* **2017**, *131*, 324–344. [CrossRef]
40. Changizi, N.; Jalalpour, M. Topology optimization of steel frame structures with constraints on overall and individual member instabilities. *Finite Elem. Anal. Des.* **2018**, *141*, 119–134. [CrossRef]
41. Zhang, G.; Khandelwal, K.; Guo, T. Finite strain topology optimization with nonlinear stability constraints. *Comput. Methods Appl. Mech. Eng.* **2023**, *413*, 116119. [CrossRef]
42. Du, J.; Olhoff, N. Topological design of freely vibrating continuum structures for maximum values of simple and multiple eigenfrequencies and frequency gaps. *Struct. Multidiscip. Optim.* **2007**, *34*, 91–110. [CrossRef]
43. Rodrigues, H.; Guedes, C.J.M.; Bendsøe, M.P. Necessary conditions for optimal design of structures with a nonsmooth eigenvalue based criterion. *Struct. Optim.* **1995**, *9*, 52–56. [CrossRef]
44. Seyranian, A.; Lund, P.E.; Olhoff, N. Multiple eigenvalues in structural optimization problems. *Struct. Optim.* **1994**, *8*, 207–227. [CrossRef]

45. Chen, X.; Qi, H.; Qi, L.; Teo, K.L. Smooth convex approximation to the maximum eigenvalue function. *J. Glob. Optim.* **2004**, *30*, 253–270. [CrossRef]
46. Torii, A.J.; Faria, J.R. Structural optimization considering smallest magnitude eigenvalues: A smooth approximation. *J. Braz. Soc. Mech. Sci. Eng.* **2017**, *39*, 1745–1754. [CrossRef]
47. Ferrari, F.; Sigmund, O.; Guest, J.K. Topology optimization with linearized buckling criteria in 250 lines of Matlab. *Struct. Multidiscip. Optim.* **2021**, *63*, 3045–3066. [CrossRef]
48. Sanders, E.D.; Ramos, A.S.; Paulino, G.H. A maximum filter for the ground structure method: An optimization tool to harness multiple structural designs. *Eng. Struct.* **2017**, *151*, 235–252. [CrossRef]
49. Parkes, E.W. Joints in optimum frameworks. *Int. J. Solids Struct.* **1975**, *11*, 1017–1022. [CrossRef]
50. He, L.; Gilbert, M. Rationalization of trusses generated via layout optimization. *Struct. Multidiscip. Optim.* **2015**, *52*, 677–694. [CrossRef]
51. Asadpoure, A.; Guest, J.K.; Valdevit, L. Incorporating fabrication cost into topology optimization of discrete structures and lattices. *Struct. Multidiscip. Optim.* **2015**, *51*, 385–396. [CrossRef]
52. Torii, A.J.; Lopez, R.H.; Leandro, L.F. Design complexity control in truss optimization. *Struct. Multidiscip. Optim.* **2016**, *54*, 289–299. [CrossRef]
53. Ohsaki, M.; Katoh, N. Topology optimization of trusses with stress and local constraints on nodal stability and member intersection. *Struct. Multidiscip. Optim.* **2005**, *29*, 190–197. [CrossRef]
54. Kanno, Y.; Fujita, S. Alternating direction method of multipliers for truss topology optimization with limited number of nodes: A cardinality-constrained second-order cone programming approach. *Optim. Eng.* **2017**, *19*, 327–358. [CrossRef]
55. Fairclough, H.; Gilbert, M. Layout optimization of simplified trusses using mixed integer linear programming with runtime generation of constraints. *Struct. Multidiscip. Optim.* **2020**, *61*, 1977–1999. [CrossRef]
56. Weldeyesus, A.G.; Gondzio, J.; He, L.; Gilbert, M.; Shepherd, P.; Tyas, A. Adaptive solution of truss layout optimization problems with global stability constraints. *Struct. Multidiscip. Optim.* **2019**, *60*, 2093–2111. [CrossRef]
57. Pedersen, N.; Nielsen, A. Optimization of practical trusses with constraints on eigenfrequencies, displacements, stresses, and buckling. *Struct. Multidiscip. Optim.* **2003**, *25*, 436–445. [CrossRef]
58. Asadpoure, A.; Harati, M.; Tootkaboni, M. Discrete topology optimization in augmented space: Integrated element removal for minimum size and mesh sensitivity control. *Struct. Multidiscip. Optim.* **2020**, *62*, 2615–2627. [CrossRef]
59. Zhou, M. Difficulties in truss topology optimization with stress and local buckling constraints. *Struct. Optim.* **1996**, *11*, 134–136. [CrossRef]
60. Movahedi Rad, M.; Habashneh, M.; Lógó, J. Reliability based bi-directional evolutionary topology optimization of geometric and material nonlinear analysis with imperfections. *Comput. Struct.* **2023**, *287*, 107120. [CrossRef]
61. Habashneh, M.; Cucuzza, R.; Domaneschi, M.; Movahedi Rad, M. Advanced elasto-plastic topology optimization of steel beams under elevated temperatures. *Adv. Eng. Softw.* **2024**, *190*, 103596. [CrossRef]
62. Wu, C.C.; Arora, J.S. Design sensitivity analysis and optimization of nonlinear structural response using incremental procedure. *AIAA J.* **1987**, *25*, 1118–1125. [CrossRef]
63. Wu, C.C.; Arora, J.S. Simultaneous analysis and design optimization of nonlinear response. *Eng. Comput.* **1987**, *2*, 53–63. [CrossRef]
64. Alberdi, R.; Zhang, G.; Li, L.; Khandelwal, K. A unified framework for nonlinear path-dependent sensitivity analysis in topology optimization. *Int. J. Numer. Methods Eng.* **2018**, *115*, 1–56. [CrossRef]
65. Sigmund, O. A 99 line topology optimization code written in matlab. *Struct. Multidiscip. Optim.* **2001**, *21*, 120–127. [CrossRef]
66. Bruggi, M. On an alternative approach to stress constraints relaxation in topology optimization. *Struct. Multidiscip. Optim.* **2008**, *36*, 125–141. [CrossRef]
67. Jiang, X.; Liu, C.; Du, Z.; Huo, W.; Zhang, X.; Liu, F.; Guo, X. A unified framework for explicit layout/topology optimization of thin-walled structures based on Moving Morphable Components (MMC) method and adaptive ground structure approach. *Comput. Methods Appl. Mech. Eng.* **2022**, *396*, 115047. [CrossRef]
68. Svanberg, K. The method of moving asymptotes—A new method for structural optimization. *Int. J. Numer. Methods Eng.* **1987**, *24*, 359–373. [CrossRef]
69. Sigmund, O.; Maute, K. Topology optimization approaches. *Struct. Multidiscip. Optim.* **2013**, *48*, 1031–1055. [CrossRef]
70. Rojas-Labanda, S.; Stolpe, M. Benchmarking optimization solvers for structural topology optimization. *Struct. Multidiscip. Optim.* **2015**, *52*, 527–547. [CrossRef]
71. Poulsen, P.N.; Olesen, J.F.; Baandrup, M. Truss optimization applying finite element limit analysis including global and local stability. *Struct. Multidiscip. Optim.* **2020**, *62*, 41–54. [CrossRef]
72. Dahlberg, V.; Dalklint, A.; Spicer, M.; Amir, O.; Wallin, M. Efficient buckling constrained topology optimization using reduced order modeling. *Struct. Multidiscip. Optim.* **2023**, *66*, 161. [CrossRef]
73. Gilbert, M.; Tyas, A. Layout optimization of large-scale pin-jointed frames. *Eng. Comput.* **2003**, *20*, 1044–1064. [CrossRef]
74. Rozvany, G.I. On symmetry and non-uniqueness in exact topology optimization. *Struct. Multidiscip. Optim.* **2011**, *43*, 297–317. [CrossRef]
75. Wang, F.; Lazarov, B.S.; Sigmund, O. On projection methods, convergence and robust formulations in topology optimization. *Struct. Multidiscip. Optim.* **2011**, *43*, 767–784. [CrossRef]

76. Ferrari, F.; Sigmund, O. Revisiting topology optimization with buckling constraints. *Struct. Multidiscip. Optim.* **2019**, *59*, 1401–1415. [CrossRef]
77. Weldeyesus, A.G.; Gondzio, J.; He, L.; Gilbert, M.; Shepherd, P.; Tyas, A. Truss geometry and topology optimization with global stability constraints. *Struct. Multidiscip. Optim.* **2020**, *62*, 1721–1737. [CrossRef]
78. Zegard, T.; Paulino, G.H. GRAND —Ground structure based topology optimization for arbitrary 2D domains using MATLAB. *Struct. Multidiscip. Optim.* **2014**, *50*, 861–882. [CrossRef]